Nano Research

Open Access

Research Article

Selective hydrodeoxygenation of lignin-derived 2,6-dimethoxy-1,4-benzoquinone to 1,4-cyclohexanediol via Ru/CeO_2 catalyst in water

Yuxin Gao[1,3], Jinling Cheng[2]✉, Xinqi Chen[2], Rui Liu[2], Zhenzhen Sun[1,3], Xiangwen Liu[2]✉, and Zhuohua Sun[1,3]✉

[1] *State Key Laboratory of Efficient Production of Forest Resources, Beijing Forestry University, Beijing 100083, China*
[2] *Institute of Analysis and Testing, Beijing Academy of Science and Technology (Beijing Center for Physical and Chemical Analysis), Beijing 100094, China*
[3] *Hebei Key Laboratory of Agricultural and Forestry Biomass Materials Science and Application, Beijing Forestry University, Xiong'an 070001, China*

Cite this article: *Nano Research*, **2026**, *19*, 94908659. https://doi.org/10.26599/NR.2026.94908659

ABSTRACT: The selective valorization of lignin-derived quinones into high-value aliphatic alcohols is a sustainable yet challenging route for biomass upcycling, particularly in environmentally benign media. Herein, we report a robust catalytic strategy for the selective hydrodeoxygenation (HDO) of 2,6-dimethoxy-1,4-benzoquinone (DMBQ) to 1,4-cyclohexanediol (CHDO) in neat water. Using a wet-chemical approach, ultra-small ruthenium (Ru) nanoclusters were precisely engineered onto rod-shaped CeO_2 supports. The resulting Ru/CeO_2 catalyst, with a low Ru loading of ~ 0.97 wt.%, achieves an unprecedented CHDO yield of 96.7% at 200 °C and 2 MPa H_2, significantly outperforming current benchmarks involving organic solvents. Advanced characterizations (aberration corrected-high-angle annular dark-field scanning transmission electron microscopy (AC-HAADF-STEM) and X-ray absorption fine structure (XAFS)) reveal that strong metal–support interactions (SMSI) stabilize the Ru nanoclusters and generate abundant interfacial oxygen vacancies. These sites work synergistically to activate C–O bonds, facilitating a kinetically preferred "deoxygenation-before-saturation" pathway that suppresses over-hydrogenated byproducts. This study not only overcomes the limitations of poor solubility and low selectivity in aqueous systems but also provides atomic-level insights into designing cluster-based catalysts for complex biomass transformations.

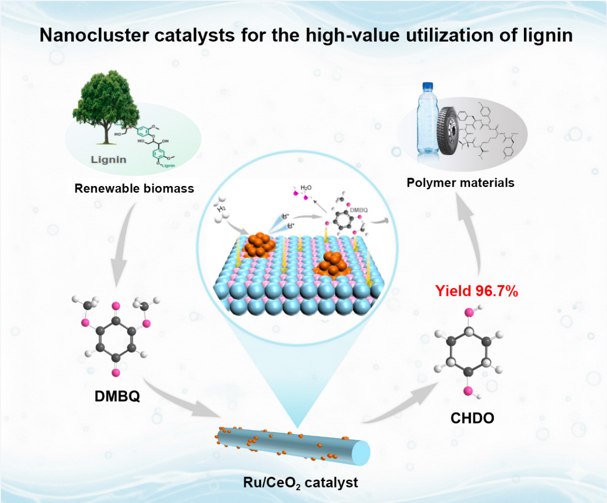

KEYWORDS: lignin, nanocluster catalysis, 1,4-cyclohexanediol, 2,6-dimethoxy-1,4-benzoquinone, Ru/CeO_2

1 Introduction

Lignocellulose, distinguished by its biodegradability, renewability, and sustainability, represents a promising alternative to petroleum-based materials [1]. Composed primarily of cellulose (30%–50%), hemicellulose (20%–35%), and lignin (15%–30%), it is the most abundant raw material on Earth. However, the conventional pulp and paper industry predominantly targets the cellulose fraction, leaving vast quantities of hemicellulose and lignin underutilized [2, 3]. In recent years, significant efforts have been directed toward the valorization of lignin, including its transformation into high-performance carbon materials [4, 5], polymers and resins [6–8], and functionalized materials [9, 10], as well as its catalytic degradation [11–15]. Among these strategies, catalytic depolymerization has attracted considerable attention from both academia and industry due to its potential for product controllability and mild reaction conditions. Prominent approaches include reductive catalytic fractionation (RCF) [12, 13, 16], oxidative degradation [17], enzymatic degradation [18, 19], and photo/electrocatalysis [20, 21].

Oxidative depolymerization stands out as a premier strategy for lignin valorization. Through catalytic oxidation, both labile C–O

Received: January 27, 2026; **Revised:** March 11, 2026
Accepted: March 22, 2026

✉Address correspondence to Jinling Cheng, JLCheng0927@163.com; Zhuohua Sun, sunzhuohua@bjfu.edu.cn; Xiangwen Liu, liuxiangwen@bcpca.ac.cn

bonds and recalcitrant C–C linkages within the lignin framework can be effectively cleaved to yield high-value aromatic monomers. Among these, 2,6-dimethoxy-1,4-benzoquinone (DMBQ) has emerged as a versatile platform molecule, valued for its biological activity and synthetic potential. Recent studies have demonstrated sophisticated control over DMBQ synthesis. For instance, Wasserscheid et al. utilized a $Mn(NO_3)_2$ catalyst in [EMIM][CF_3SO_3] ionic liquid to shift the oxidative selectivity from syringaldehyde toward DMBQ, isolating the pure product in 11.5 wt.% yield [22]. Similarly, Samec et al. employed a 2,2,6,6-tetramethylpiperidine 1-oxyl (TEMPO)-mediated strategy targeting C–C bond cleavage in high-molecular-weight lignin, which increased monomeric yields by 32% with exceptional selectivity for DMBQ [23]. Furthermore, Kim et al. reported a sustainable enzymatic route using recombinant lignin peroxidase (PcLiP01) to achieve selective C–C cleavage under ambient conditions [24].

However, the direct application of DMBQ is limited; it serves primarily as an intermediate for transformation into higher-value chemical feedstocks. Building on previous work [25, 26], we identified DMBQ as a precursor for conversion into 1,4-cyclohexanediol (CHDO) via reductive demethoxylation and hydrogenation. CHDO is a valuable monomer; its distinct *cis/trans* isomerism facilitates the production of polycarbonates, polyethers, scratch-resistant polyesters, and supramolecular assemblies [27–30]. Recently, our group explored the hydrodeoxygenation (HDO) of DMBQ using commercial and modified Raney nickel catalysts. Initially, we employed Raney® Ni to effect the demethylation and hydrogenation of DMBQ, yielding CHDO (86.5%), which was subsequently converted quantitatively to 1,4-cyclohexanediamine via amination [25]. In subsequent optimization studies using a Mn-modified Raney Ni catalyst under anhydrous conditions, a CHDO yield of 86.1% was achieved in only 1 h at 200 °C [26]. Despite these advances, precise control over DMBQ hydrogenation remains challenging. Moreover, the reliance on organic solvents and anhydrous conditions in established protocols necessitates the development of more environmentally benign alternatives.

In light of these challenges, we propose the utilization of Ru, a catalyst distinguished by its stability in aqueous media and exceptional hydrogen-activating capability, to address the sustainability issues and yield limitations inherent in earlier systems [31–36]. For instance, to circumvent the limitations imposed by the inherent low aqueous solubility of hydrogen, a hydrophobic poly(divinylbenzene)-supported Ru catalyst (Ru/PDVB) was strategically engineered. This system achieved a turnover frequency for pyridine hydrogenation 6-fold higher than that of traditional Ru/C [37]. Similarly, a bifunctional Ru/$NiAl_2O_4$ catalyst effectively mediated the catalytic transfer hydrogenation of guaiacol to cyclohexanol in a water/isopropanol mixture, wherein water significantly enhanced the hydrogen exchange rate [38]. Furthermore, the aqueous-phase HDO of biomass-derived sorbitol into 1-hexanol was achieved over a multifunctional Ru-MoO_x/Mo_2C catalyst. This catalytic architecture exploited the strong synergistic interplay between Ru and Mo species to steer the site-specific cleavage of C–O bonds, thereby achieving precise deoxygenation without compromising the structural integrity of the carbon backbone [39]. Collectively, these studies underscore the versatility of Ru-based systems in facilitating efficient biomass upgrading under environmentally benign aqueous conditions. Although Ru-based catalysts have been widely applied in the aqueous hydrogenation of biomass, previous studies have focused on adding partial organic solvents or achieving only partial hydrogenation. It has been challenging to directly obtain high-yield deep hydrogenation products in pure water systems. CeO_2 was selected as the support due to its exceptional oxygen storage capacity and the ease of forming surface oxygen vacancies, which can synergistically interact with Ru clusters to create active interfacial sites for the efficient activation of C–O bonds [40–42].

Herein, we report a highly efficient and environmentally benign strategy for the direct HDO of DMBQ to CHDO, utilizing water as the sole solvent (Fig. 1). Distinguished from conventional Ru-based systems that often yield over-hydrogenated byproducts or require organic solvents, we demonstrate that Ru nanoclusters, anchored on rod-shaped CeO_2 supports, achieve an unprecedented CHDO yield of 96.7%. Using aberration-corrected high-angle annular dark-field scanning transmission electron microscopy (AC-HAADF-STEM) and synchrotron-based X-ray absorption fine structure (XAFS) spectroscopy, we reveal that a robust strong metal–support interactions (SMSI) not only stabilizes the Ru nanoclusters against sintering but also significantly reconfigures the interfacial coordination environment. This precise electronic modulation enhances the synergistic activation of C–O bonds via interfacial oxygen vacancies (O_v) and hydrogen species adsorbed on Ru sites. By integrating high chemoselectivity with a sustainable aqueous process, this study not only presents a high-performance catalyst for lignin valorization but also provides atomic-level insights into the rational design of cluster-based catalysts for complex biomass transformations.

2 Results and discussion

2.1 Preparation and characterization of catalysts

We employed a wet chemical method to load Ru in the form of nanoclusters onto hydrothermally synthesized nano-rod CeO_2. Scanning electron microscopy (SEM) and transmission electron microscopy (TEM) characterization demonstrates that the as-synthesized CeO_2 material exhibits a uniform rod-like morphology, with the nanorods having average diameters and lengths on the order of hundreds of nanometers (Figs. 2(a) and 2(b), and Fig. S4 in the Electronic Supplementary Material (ESM)). And further high-resolution structural analysis via AC-HAADF-STEM for the CeO_2 nanorods unveils a distinct lattice spacing of 0.31 nm, which corresponds to the (111) crystallographic plane of CeO_2 nanorods (Fig. 2(c)). Additionally, the presence of the (110) crystal plane was partially observed. Compared to other CeO_2-shaped structures, nanorods exhibit significantly lower formation energies for oxygen vacancies on exposed (110) crystal planes. This crystal plane-dependent property promotes the generation of high-concentration interfacial oxygen vacancies [43, 44]. After the introduction of Ru nanoclusters, the structural characterization of the Ru/CeO_2 catalyst was performed (Figs. 2(d) and 2(e), and Fig. S5 in the ESM). It was observed that CeO_2 retained its original crystal plane structure. Furthermore, leveraging the inherent Z-contrast imaging principle of AC-HAADF-STEM, where signal intensity is proportional to the atomic number, sub-nanometer Ru clusters consisting of several to tens of Ru atoms were clearly visualized on the CeO_2 support surface, with an average diameter of 1.6 ± 0.2 nm. The existence of these Ru clusters within the Ru/CeO_2 catalyst architecture was further corroborated by energy-dispersive X-ray spectroscopy (EDS) analyses, which detected a distinct yet low-intensity Ru

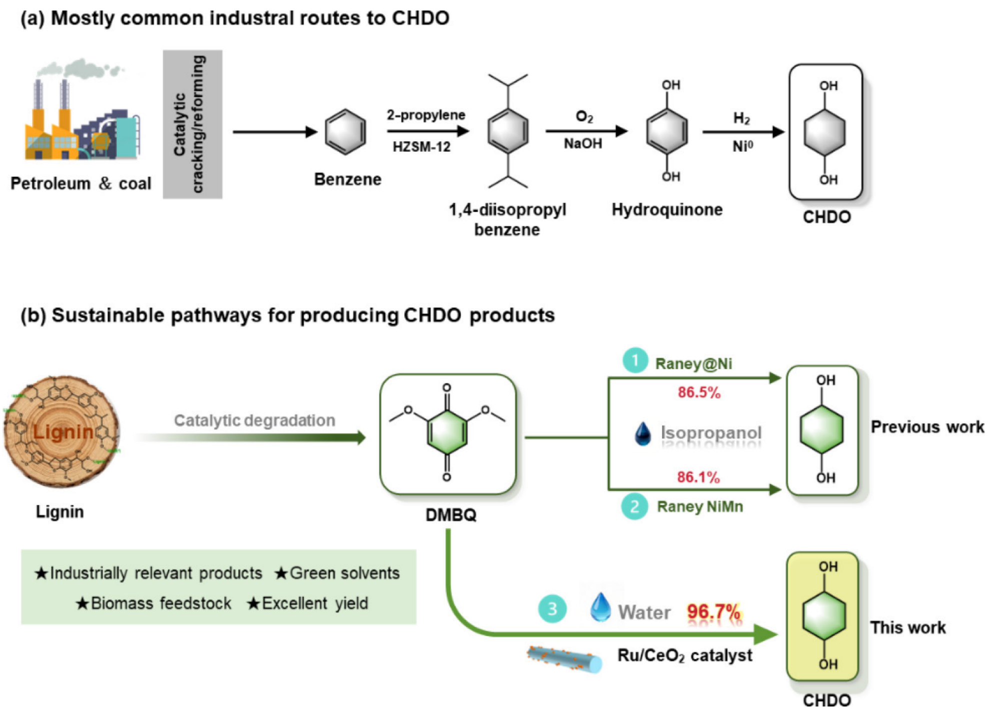

Figure 1 Existing industrial strategies and emerging sustainable approaches for CHDO production. (a) Traditional industrial and prospective pathways to produce CHDO, with the central starting compound being fossil-derived benzene. (b) Generating CHDO via the lignocellulosic biomass pathway: (1) demethoxylation and hydrogenation of DMBQ to CHDO over Raney@Ni catalyst [25], and (2) demethoxylation and hydrogenation of DMBQ to CHDO over RANEY NiMn catalyst [26]. (3) This paper proposes the generation of CHDO in an aqueous solvent system using Ru/CeO_2 catalyst.

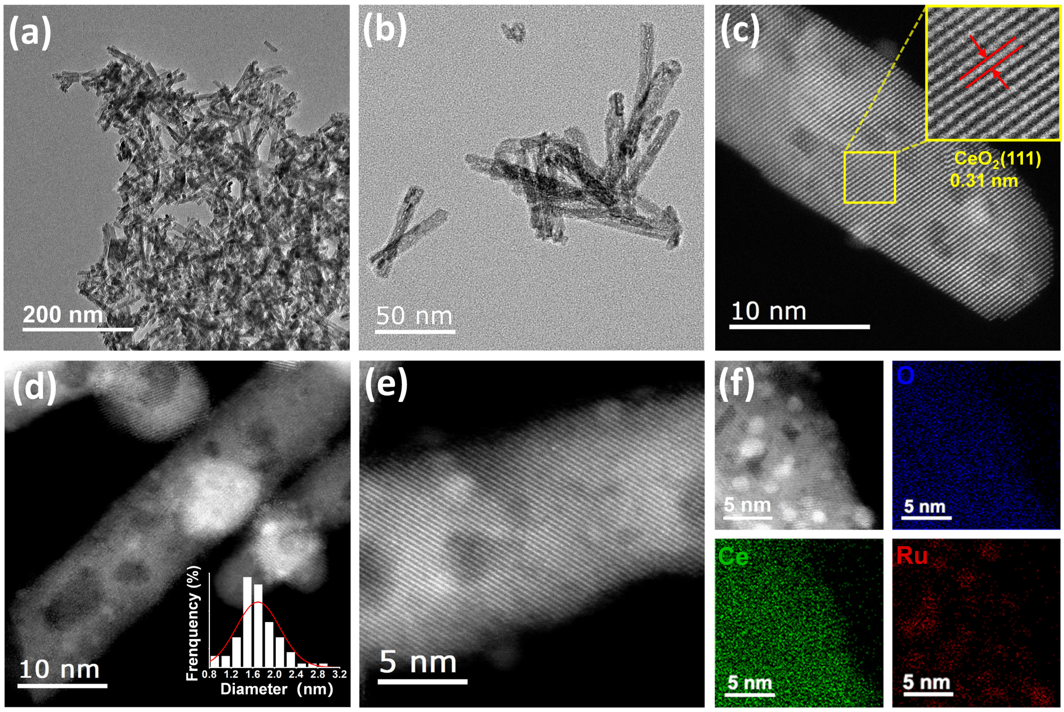

Figure 2 Morphology and elemental distribution analysis of Ru/CeO_2. ((a) and (b)) TEM images. ((c)–(e)) AC-HAADF-STEM images and statistical histograms of Ru particle size distribution (based on $n = 100$ particles). (f) elemental mapping under AC-HAADF-STEM.

characteristic signal (Fig. 2(f)). The actual Ru loading on the CeO_2 nanorods was quantified via inductively coupled plasma optical emission spectroscopy (ICP-OES) analysis as 0.968 wt.%, which is in good agreement with the nominal loading of 1.0 wt.%.

X-ray diffraction (XRD) pattern (Fig. 3(a)) indicates that as-prepared Ru/CeO_2 is indexable to the cubic fluorite phase as distinct diffraction peaks at 28.6°, 33.1°, 47.5°, 56.3°, 59.1°, 69.4°, 76.7°, 79.1°, and 88.4° corresponding to the (111), (200), (220), (311), (222), (400), (331), (420), and (422) planes of CeO_2, respectively (JCPDS No. 34-0394). Notably, no characteristic diffraction peaks assignable to crystalline metallic Ru (e.g., the signature peak at $2\theta = 44°$ for Ru nanoparticles) or RuO_2 ($2\theta = 28°$) phases are detected in the XRD

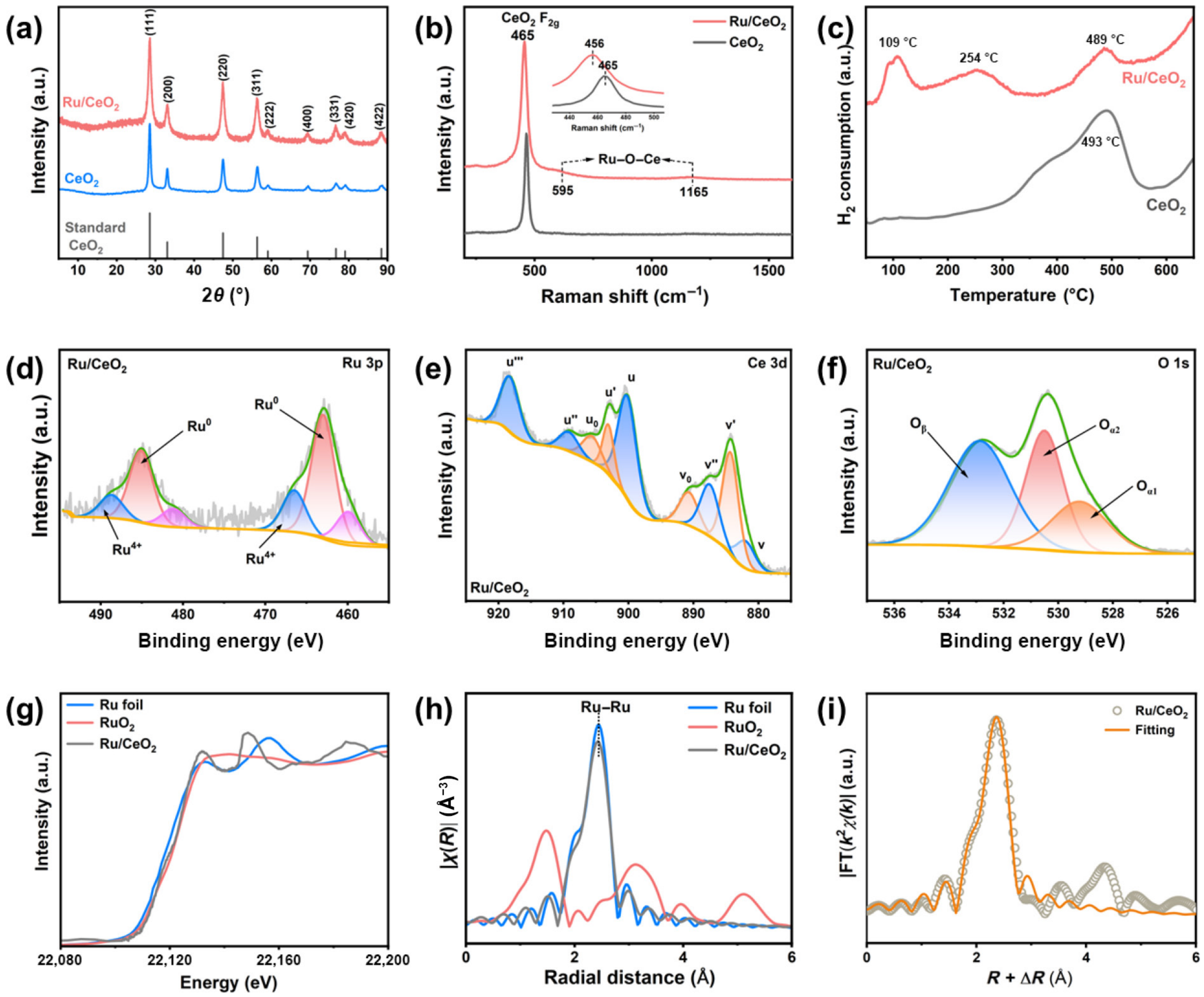

Figure 3 (a) XRD patterns of Ru/CeO$_2$ and CeO$_2$ compared with standard CeO$_2$ (JCPDS No. 34-0394). (b) Raman spectra. (c) H$_2$-TPR profiles of Ru/CeO$_2$ and CeO$_2$. ((d)–(f)) High-resolution XPS spectra for (d) Ru 3p, (e) Ce 3d, and (f) O 1s. ((g)–(i)) XAFS analysis: (g) the XANES K-edge spectra, (h) Fourier-transformed (FT) EXAFS spectra in *R*-space, and (i) EXAFS curve-fitting at Ru-edge of Ru/CeO$_2$.

pattern. This absence suggests that the Ru species are uniformly anchored on the CeO$_2$ nanorods with a small particle size, consistent with the direct observations from HAADF-STEM. The structural evolution and lattice defect characteristics of the fabricated catalysts are systematically probed via Raman spectroscopy (Fig. 3(b)). For the pristine CeO$_2$ nanorods, a prominent F$_{2g}$ symmetric stretching vibration band centered at 465 cm^{-1}, which is consistent with the characteristic Raman feature of fluorite-structured CeO$_2$ [36]. Following Ru loading, this F$_{2g}$ band experiences a distinct blue shift to 456 cm^{-1}, coupled with marked peak broadening. Such spectral perturbations are direct spectroscopic evidence of significant lattice strain engendered by the incorporation of Ru species into the CeO$_2$ lattice, which distorts the local atomic arrangement and perturbs the symmetry of the CeO$_2$ fluorite structure [45]. The calculated $I_D/I_{F_{2g}}$ ratio rose from 0.1 for pure CeO$_2$ to 0.4 for Ru/CeO$_2$, quantitatively confirming the enriched concentration of oxygen vacancies generated at the Ru-ceria interface. Most notably, three faint Raman bands centered 260, 595, and 1165 cm^{-1} are assigned to the second-order transverse acoustic (2TA) mode, the defect-induced mode (D), and the second-order longitudinal optical (2LO) mode, respectively [46]. Subsequent to Ru loading, two new distinct Raman peaks emerge at 559 and 1165 cm^{-1}, which can be attributed to the generation of Ru-induced oxygen vacancies and the formation of Ru–O–Ce interfacial structures, respectively [47].

Fourier transform infrared (FT-IR) spectroscopy (Fig. S6 in the ESM) examined changes in surface functional groups, and the surface hydroxyl (–OH) signal near 3420 cm^{-1} weakened after loading, indicating that Ru nanoclusters preferentially interact with hydroxyl groups on the support surface. Notably, Ru/CeO$_2$ exhibits a new and weak absorption peak near 1165 cm^{-1}, typically attributed to vibrational modes arising from localized lattice perturbations or interfacial species induced by metal loading. The H$_2$ temperature-programmed reduction (H$_2$-TPR) spectrum (Fig. 3(c), and Tables S1 and S2 in the ESM) demonstrates the significant enhancement of Ru on the reduction performance of the CeO$_2$ surface. Pure CeO$_2$ exhibits typical surface oxygen reduction only at 400–500 °C, whereas the Ru/CeO$_2$ catalyst shows markedly enhanced reduction processes driven by the hydrogen overflow effect. The sharp peak at 109 °C originates from highly active Ru–O–Ce interfacial oxygen; the peak at 254 °C corresponds to Ru-induced surface oxygen (Ru–O–Ce–O); and the peak around 498 °C represents the extensive reduction of subsurface oxygen on CeO$_2$ [48]. This low-temperature reduction behavior confirms the presence of strong metal–support interactions, which favor the dynamic formation of active oxygen vacancies.

X-ray photoelectron spectroscopy (XPS) was further implemented to clarify the surface compositions and valence states of the obtained Ru/CeO_2 catalyst. Given the spectral overlap between Ru 3d and C 1s core-level signals, the Ru 3p XPS measurements were performed instead to unambiguously resolve the valence states of Ru species. The deconvoluted Ru 3p spectrum reveals two distinct ruthenium species (Fig. 3(d)). The dominant peaks at 462.84 and 484.99 eV are attributed to the orbitals of metallic Ru^0, confirming the abundance of reduced active metal centers. Additionally, the component at a higher binding energy of is attributed to Ru^{4+} species. This suggests a slight surface oxidation of Ru nanoclusters or an interfacial electron transfer from Ru to the CeO_2 support induced by strong metal–support interactions [49, 50]. Moreover, in the Ce 3d spectrum (Fig. 3(e)), the characteristic v^0, v', u^0, and u' satellite peaks for Ce^{3+} are clearly observed. Compared to the pure CeO_2 carrier, the Ce peak shifted toward higher binding energies, and the proportion of Ce^{3+} increased significantly from 0.33 to 0.50 (Table S3 in the ESM), indicating that ruthenium loading significantly promotes the reduction of surface Ce^{4+} to Ce^{3+}. The unique electronic configuration of Ce enables reversible redox interconversion between the Ce^{4+} and Ce^{3+} states in CeO_2; during this valence transition process, active oxygen species are liberated to preserve charge neutrality, and the resulting oxygen vacancies can subsequently be compensated by oxygen-bearing moieties such as O_2, H_2O, and CO_2 [51]. Concomitantly, the O 1s spectrum (Fig. 3(f)) displays a prominent O_β peak at a binding energy of 532.8eV, which is attributable to surface-adsorbed oxygen species associated with oxygen vacancies [52]. The high relative proportion of O_β component is consistent with the existence of Ce^{3+} species in the catalyst matrix. After loading Ru, the O_β peak percentage significantly increased from 0.68 to 2.26 (Table S3 in the ESM), and its binding energy exhibited a pronounced shift toward higher energies. This trend, coupled with the simultaneous increase in Ce^{3+} concentration, confirms that strong metal–support interactions promote the formation of interfacial oxygen vacancies [53].

The chemical state and coordination environment of the Ru/CeO_2 catalyst were examined by X-ray absorption near-edge structure (XANES) and extended X-ray absorption fine structure (EXAFS) spectroscopy. As shown in Fig. 3(g), the Ru K-edge XANES spectra demonstrate that the absorption edge position of Ru/CeO_2 is consistent with that of the Ru foil standard, confirming the predominantly metallic state of the Ru species after reduction. Subsequently, in the *R*-space EXAFS spectra (Fig. 3(h) and Table S4 in the ESM), a prominent characteristic peak observed at approximately 2.67 Å is assigned to the metallic Ru–Ru shell scattering, while no significant Ru–O coordination peak is detected. Although Raman spectroscopy indicated the presence of interfacial Ru–O–Ce bonds, the absence of a dominant Ru–O scattering path in EXAFS suggests that these interfacial species constitute a minor fraction compared to the metallic Ru core. Furthermore, the Ru–Ru peak in Ru/CeO_2 shows significantly lower intensity and a smaller coordination number (CN) compared to the Ru foil, indicating the highly dispersed nature of the Ru species on the support. Figure 3(i) presents the corresponding coordination curve derived from fitting the experimental data. Notably, although H_2-TPR suggests the reduction of Ru species at relatively low temperatures, a distinct Ru–O coordination shell is still observed in the EXAFS fitting results.

In summary, multiple structural characterizations collectively demonstrate that highly dispersed Ru nanoclusters are stably anchored on the surface of defective CeO_2 nanorods. Through strong metal–support interactions, these Ru clusters not only induce the formation of a high concentration of interfacial oxygen vacancies but also significantly enhance the redox properties and electron transfer efficiency of the system. This provides a robust structural foundation for the low-energy-barrier dissociation of hydrogen molecules and the oriented polarization-activated adsorption of substrate molecules during the reaction.

2.2 Catalytic performance evaluation

Following the comprehensive structural characterization, subsequent efforts were directed toward the catalytic activity screening and the systematic optimization of reaction parameters. To verify the unique role of the CeO_2 nanorod support, reference catalysts including Ru/SiO_2, Ru/TiO_2, and Ru/ZrO_2 were prepared and evaluated under the same conditions (Table S5 in the ESM). Although these reference catalysts showed varying degrees of activity, their selectivity toward the target product CHDO was significantly lower than that of Ru/CeO_2. Specifically, Ru/ZrO_2 and Ru/TiO_2 primarily yielded intermediate species and partial hydrogenation products. The primary product of Ru/SiO_2 is CHDO, but its selectivity is insufficient. To demonstrate the rationality of Ru metal loading, we evaluated a series of catalysts with varying Ru loadings, and 1.0 wt.% Ru emerged as the optimal choice, achieving maximized interfacial active sites while maintaining high metal dispersion and cost-effectiveness. The morphology effect of CeO_2 was investigated using nanorods, nanosheets, and nanocubes, and nanorods exhibit the best catalytic performance (Table S6 and Fig. S10 in the ESM).

After that, we compared the performance of commercial catalysts with Ru/CeO_2 catalysts under identical conditions (Fig. 4(a)), revealing that the Ru/CeO_2 catalyst demonstrated significantly superior product selectivity compared to the commercial catalyst. While noble metal catalysts (e.g., Pd/C, Ru/C, and Pt/C) showed hydrogenation capabilities, they suffered from poor selectivity, generating complex mixtures and over-hydrogenated byproducts cyclohexanol (3A). This suggests that traditional carbon-based supports lack the necessary selective activation for specific functional groups. Furthermore, non-precious metal catalysts (Raney Ni and Ni/Al_2O_3-SiO_2) primarily remained at the intermediate stage, struggling with the deoxygenation of sterically hindered methoxy (–OMe) groups. In contrast, the Ru/CeO_2 nanoclusters facilitated complete conversion to CHDO, highlighting the unique role of the CeO_2 support in directing the reaction pathway.

Given the limited solubility of DMBQ in water, increasing the temperature facilitates complete dissolution of the substrate (Fig. 4(b)). Therefore, temperature is prioritized as the primary factor for investigation. When the temperature is below 160 °C, the active hydrogen generated from the dissociation of Ru nanoclusters preferentially attacks the carbonyl oxygen, resulting in a low reaction conversion rate and a product dominated by DMHQ. As the temperature increased, pronounced C–OMe bond cleavage (demethoxylation) coupled with the saturation of the aromatic moiety occurred, consequently yielding a substantial enrichment of the CHDO fraction. At 200 °C, the CHDO yield reaches its maximum value. As the temperature further increases to 220 °C, a discernible diminution in CHDO selectivity is observed, while the proportion of byproduct cyclohexanol rises. Time is also a crucial

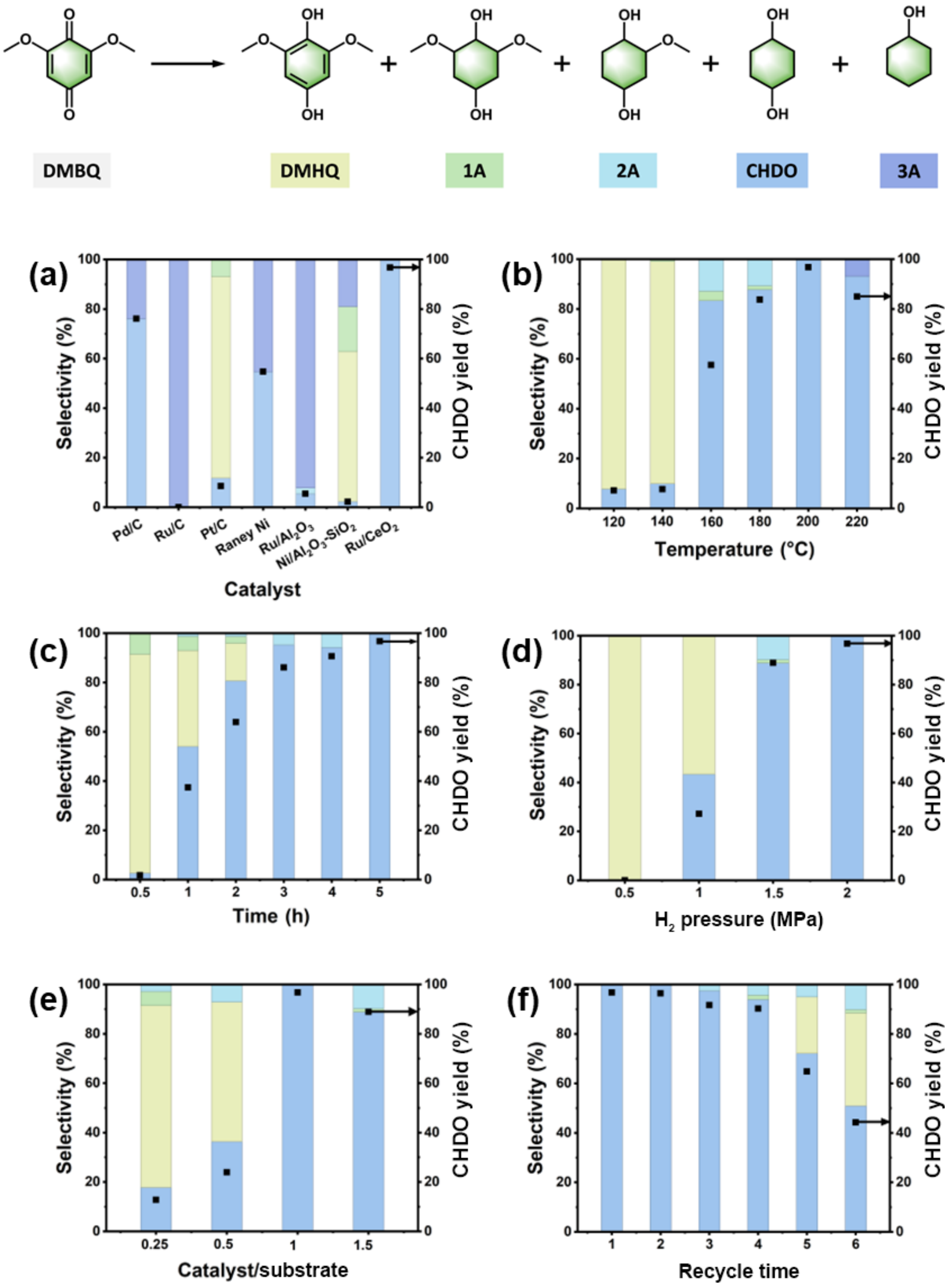

Figure 4 Establishment of the optimal reaction conditions for the catalytic conversion of DMBQ to CHDO. (a) Yield and product distribution of CHDO under different commercial catalysts. (b) Reactions at different temperatures. (c) Reactions under different time. (d) Reactions under different H_2 pressures. (e) Reactions under different catalyst/substrate ratios. (f) Recycling test. For specific data in the image, please refer to Tables S7–12 in the ESM.

factor influencing the catalytic reaction (Fig. 4(c)). It can be observed that during the initial reaction phase, DMHQ predominates in the products, indicating that the hydrogenation of the C=O bond occurs extremely rapidly. As time progressed, the cleavage of the C–OMe bond (demethylation) proceeded concurrently with the hydrogenation of the C=C bond (benzene ring saturation). After 3 h, the selectivity of CHDO approached 95%. At approximately 5 h, the yield of CHDO reached its maximum value (96.7%). Hydrogen pressure is the decisive factor in determining whether the reaction can transition from “hydrogenation” to “deep deoxygenation” (Fig. 4(d)). Under low hydrogen pressure, the active hydrogen coverage on the Ru cluster surface is insufficient. While sufficient to saturate the C=O bond, it fails to provide adequate energy to cleave the higher-energy C–OMe bond, resulting in nearly all products remaining at the DMHQ stage. Upon increasing the pressure to 1.5 MPa, the CHDO yield surged; at 2 MPa, DMHQ completely disappeared, achieving complete conversion. This may be attributed to high pressure significantly promoting H_2 and enhancing the hydrogen overflow effect, thereby overcoming the activation energy barrier for C–O bond cleavage. Finally, the influence of the catalyst-to-substrate mass ratio on the catalytic performance was systematically investigated (Fig. 4(e)). When the ratio was 1.0, the rate of active hydrogen provided by the catalyst reached a synergistic equilibrium with the activation rate of the methoxy group, resulting in a peak CHDO yield. The reusability of the Ru/CeO_2 catalyst was investigated. To ensure the accuracy and validity of the catalyst stability results, two parallel reaction sets were conducted simultaneously to collect additional spent catalysts for subsequent experiments. As shown in Fig. 4(f), after three reuse cycles, the CHDO yield remained above 90%, fully demonstrating the exceptional stability of Ru/CeO_2. The spent catalyst collected after four consecutive runs was characterized using XRD and HAADF-STEM techniques (Fig. S11 in the ESM). The average size of ruthenium nanoclusters slightly increased compared to fresh catalysts, indicating the onset of surface sintering under hydrothermal conditions. This aggregation phenomenon may reduce the density of Ru–O_v interface active sites, thereby affecting DMBQ activation. Concurrently, XRD analysis of spent catalysts showed no significant changes in the ceria diffraction peaks, suggesting that the carrier morphology and crystallinity were well preserved.

2.3 Investigation of reaction mechanisms

The conversion of DMBQ to CHDO proceeds through multiple simultaneous and sequential reaction steps, including hydrogenation and demethoxylation. To quantitatively decipher this complex reaction network, a series of model compound studies were conducted using individual compounds: DMBQ, DMHQ, 2,6-dimethoxy-1,4-cyclohexanediol (1A), 2-methoxy-1,4-cyclohexanediol (2A), 2-methoxy-1,4-benzenediol (1H), and 1,4-benzenediol (2H). Kinetic experiments were systematically carried out for each substrate within a temperature range of 160–200 °C to determine their respective apparent activation energies (E_a) (Table S19 in the ESM). As illustrated in the Arrhenius plots (Fig. S12 in the ESM), all substrates exhibited high linear correlation coefficients, indicating a consistent catalytic behavior across the investigated temperature regime.

As shown in Fig. 5(a), DMBQ undergoes rapid conversion within 1 h, showing an extremely fast disappearance rate accompanied by the rapid generation of DMHQ. These findings substantiate that the catalytic hydrogenation of the carbonyl moiety represents the most kinetically preferred primary step, supported by the low activation energy of 17.99 kJ/mol for DMHQ. Subsequently, the reaction proceeds via two pathways: Pathway A involves removal of the methoxy group to yield 1H, while pathway B involves hydrogenation of the benzene ring to yield 1A. However, kinetic experiments indicate (Fig. 5(b)) that when DMHQ serves as the substrate, it predominantly stabilizes as the demethylated product (1H), with only a negligible amount of product 1A formed. This confirms DMHQ as the key platform intermediate where aromatic-state deoxygenation dominates over saturation. When we continued using 1H (Fig. 5(c)) and 2H (Fig. 5(d)) as substrates, the formation rate of CHDO was significantly accelerated. The subsequent benzene ring saturation of 2H is even faster, consistent with its minimal E_a of 17.82 kJ/mol, the target product can be obtained through benzene ring hydrogenation within an extremely short time. It is noteworthy that the concentrations of intermediates 1H and 2H remain extremely low throughout the overall conversion, which is primarily attributed to their extremely high reactivity. In stark contrast, intermediates 1A (Fig. 5(e)) and 2A (Fig. 5(f)) cannot be fully converted to CHDO even within 5 h. Calculations reveal that the activation energy for the conversion of 2A to CHDO (68.52 kJ/mol) is nearly four times that of the conversion of 2H to CHDO (17.82 kJ/mol), which accounts for the extremely slow rate of pathway B. It is noteworthy that although the apparent activation energy of 1A is lower than that of 1H, its absolute reaction rate is remarkably reduced due to weak adsorption of saturated structures and low reaction frequency. This indicates that the removal of the methoxy side chain becomes extremely difficult, likely due to increased steric hindrance and C–O bond activation energy. Consequently, based on the kinetic analysis, we conclude that the HDO of DMBQ follows an optimal pathway of "deoxygenation-first, saturation-second" (Fig. (6)).

We attribute the superior HDO performance and notable kinetic preference exhibited by the Ru/CeO_2 catalyst to the synergistic interplay between ultrasmall Ru nanoclusters and the defective CeO_2 support. In the catalytic hydrogenation cycle, the dissociative adsorption of H_2 molecules constitutes the foundational step that governs the initial reaction kinetics. Regarding the hydrogen activation mechanism over Ru-based catalysts, recent theoretical studies have underscored the decisive influence of Ru species size and coordination environment on the energy barrier for H_2 dissociation. Tang et al. [54] compared various Ru configurations via DFT calculations and revealed that Ru clusters with adjacent metallic sites exhibit significantly lower dissociation barriers than isolated single atoms. Concurrently, the work by Zhang et al. [55] and Yang et al. [56] further confirmed that ultrafine Ru nanoclusters (1.2–2.7 nm) anchored on supports act as super-active centers for H_2 activation; moreover, they substantially enhanced the hydrogen spillover effect by lowering the migration resistance of active hydrogen (H*) across the interface through strengthened electronic coupling. Building upon these theoretical frameworks, we propose that the exceptional hydrogenation activity of our Ru/CeO_2 catalyst originates from the presence of highly dispersed Ru nanoclusters. At a relatively low reduction temperature (109 °C), H_2 molecules preferentially undergo efficient polarization and dissociation on these clusters featuring adjacent coordination-unsaturated sites. The resulting H* atoms then traverse the Ru–CeO_2 interface and rapidly spill over to the oxygen vacancies on the support surface. This efficient hydrogen dissociation and spillover pathway, mediated by Ru clusters, provides a continuous and abundant supply of active hydrogen for DMBQ conversion, theoretically rationalizing the rapid initial reaction rates observed experimentally. In heterogeneous catalysis, the directional adsorption configuration of substrate molecules and the pre-activation of their key chemical bonds are the primary factors determining reaction kinetics. For DMBQ, which possesses a highly symmetric quinone structure, its carbonyl oxygen atoms tend to preferentially attack the Lewis acid sites on the catalyst surface due to their significant electronegativity and lone pair electrons. Recent studies by Zhu et al. [57] and Zhao et al. [43] collectively revealed the pivotal role of O_v on ceria-based supports in activating carbonyl (C=O) groups. Their theoretical calculations demonstrated that the carbonyl oxygen can spontaneously "fill" the asymmetric O_v on the surface. This robust chemisorption induces electron transfer from the support to the anti-bonding orbitals of the C=O bond, leading to significant polarization and physical elongation of the bond. Drawing on this mechanistic logic and supported by the experimental fact of a substantially increased O_β fraction in our XPS characterization, it is proposed that during the initial stage of DMBQ conversion, the carbonyl oxygen is first anchored onto the O_v at the Ru/CeO_2 interface. This adsorption configuration not only enhances substrate capture but also weakens the C=O bond

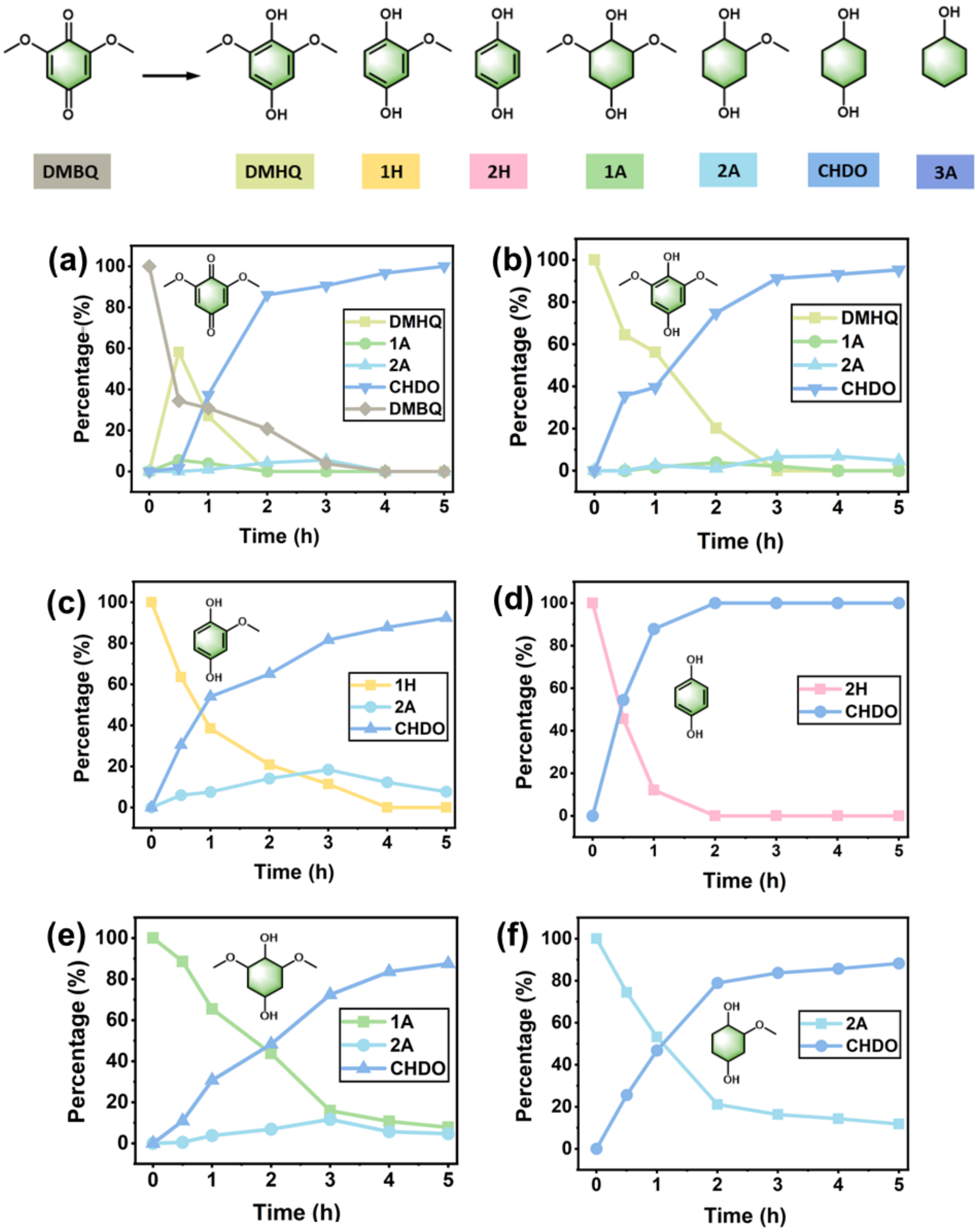

Figure 5 Transformation of various intermediates with Ru/CeO_2 catalyst. Reaction conditions: 0.01 g of reactants, 0.01 g of Ru/CeO_2 catalyst, 3 mL of H_2O, 200 °C, and 2 MPa H_2. (a) With substrate DMBQ. (b) With substrate DMHQ. (c) With substrate 1H. (d) With substrate 2H. (e) With substrate 1A. (f) With substrate 2A. For specific data in the image, please refer to the Tables S13–18 in the ESM.

strength through polarization, making it a privileged site for attack by active hydrogen (H*). Therefore, DMBQ initially undergoes carbonyl hydrogenation to form the DMHQ intermediate, a process in which oxygen vacancies play a crucial role in significantly lowering the reaction energy barrier. Following the conversion of DMBQ to the intermediate DMHQ, the precise cleavage of C–O bonds on the benzene ring for deep deoxygenation is the pivotal step governing product distribution. Regarding the deoxygenation essence of ceria-based catalysts, Ding et al. [58] pointed out that the concentration of surface O_v on CeO_2 directly defines its Lewis acidity, which significantly polarizes the C–O bonds in oxygenated functional groups through strong chemisorption. Furthermore, Shang et al. [44] confirmed via DFT calculations that CeO_2 nanorods exposing facets can induce highly active interfacial O_v through SMSI. These sites synergize with oxophilic Ru species to cause substantial elongation of the C–Ar bond in methoxy groups (–OCH_3) via the "oxygen-filling" effect, thereby preferentially driving the direct deoxygenation pathway over aromatic ring hydrogenation. Building upon the above research, it is proposed that in the present system, DMHQ molecules first anchor onto the high-density oxygen vacancies and associated Lewis acid sites on the carrier surface via the oxygen atom of the methoxy group. This adsorption configuration induces electron cloud redistribution and bond elongation in the methoxy C–O bond, placing it in a highly activated and pre-dissociation state.

Subsequently, active hydrogen species (H*) continuously generated from neighboring Ru clusters rapidly migrate to this interface site and attack the activated methoxy carbon atom, ultimately leading to the stepwise removal of the methoxy groups. Following the stepwise removal of methoxy groups to yield

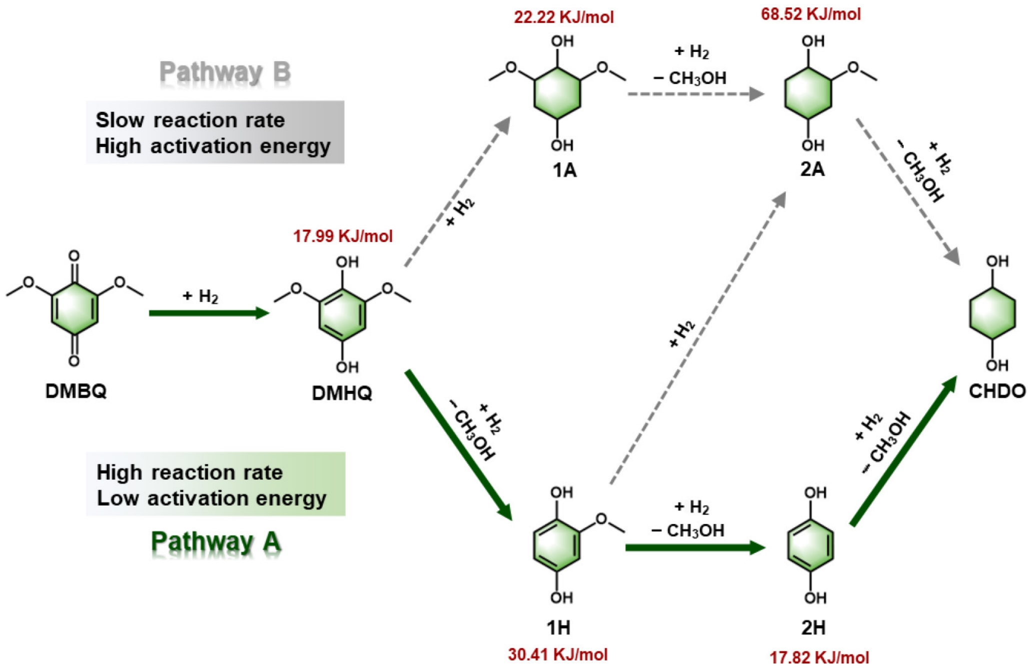

Figure 6 Proposed reaction network for the catalytic hydrogenation of DMBQ over Ru/CeO_2.

hydroquinone, the subsequent step involves the activation and hydrogenation of the quinone ring system at the active site. The study by Wang et al. [59] on fully exposed Ru clusters demonstrated that atomically dispersed Ru clusters, with an optimized d-band center, can exhibit moderate interaction with the π-orbitals of aromatic rings, thereby significantly accelerating the hydrogen transfer kinetics during multi-step hydrogenation. We propose that the highly dispersed Ru clusters in our Ru/CeO_2 catalyst play a dual role in the sequential deoxygenation of DMHQ. On the one hand, the Ru clusters serve as an efficient "hydrogen factory", providing a nearly barrier-less pathway for H_2 dissociation. On the other hand, their fully exposed surface structure enhances the capture of aromatic intermediates. Facilitated by the pre-activation of C–O bonds by CeO_2 oxygen vacancies, the abundant active hydrogen supplied by Ru clusters can rapidly diffuse across the interface to attack the activated sites. This combination of efficient hydrogen utilization and cyclic substrate activation explains why DMBQ can transcend multiple intermediate steps and convert into deeply deoxygenated products with an explosive initial rate.

In previous studies, the Raney nickel catalytic system relied primarily on non-specific strong adsorption of carbonyl groups and benzene ring π-electron clouds onto the nickel metal surface. Although demonstrating excellent hydrogenation efficiency, this system exhibited a tendency toward aromatic ring hydrogenation rather than selectively producing CHDO, due to the relatively random distribution of active sites and a lack of directed activation capability toward specific C–O bonds. In contrast, the Ru/CeO_2 system achieves superior HDO performance through interfacial synergistic effects. As illustrated in Fig. 7, the reaction initiates with the dissociative activation of H_2 on Ru nanoclusters, generating active hydrogen (H*) that migrates to the CeO_2 surface via hydrogen spillover. Simultaneously, DMBQ anchors onto interfacial O_v through its carbonyl oxygen atoms, an adsorption mode that weakens the C=O and C–O bonds for subsequent attack by spillover H*. This cooperation allows for precise deoxygenation of methoxy groups, releasing methanol (CH_3OH) and water (H_2O), before the aromatic ring undergoes final saturation on the Ru surface to yield CHDO. The synergism is crucial: Ru provides abundant active hydrogen, O_v sites directedly activate specific oxygenated groups, and the spillover effect bridges these two functions to enable an efficient and high-speed catalytic cycle.

3 Conclusions

In conclusion, a highly active and eco-friendly Ru/CeO_2 nanorod catalyst was developed for the chemoselective HDO of lignin-derived DMBQ to CHDO. By precisely engineering ultra-small Ru nanoclusters onto rod-shaped CeO_2 supports, an unprecedented CHDO yield of 96.7% was attained under mild conditions (200 °C, 2 MPa H_2) in a pure aqueous phase. Advanced structural characterization techniques, including HAADF-STEM and XAFS, confirmed that Ru species exist as highly dispersed nanoclusters and exhibit synergistic interactions with the ceria interface, jointly promoting the HDO reaction. Oxygen vacancies on the CeO_2 support serve as specific anchoring sites that capture and activate the C=O and C–O bonds of DMBQ, while the Ru nanoclusters facilitate hydrogen dissociation and benzene ring hydrogenation. Kinetic evidence indicates that this process preferentially follows a "deoxygenation-before-saturation" pathway, which effectively regulates the hydrogenation depth and suppresses the formation of over-hydrogenated byproducts. Compared to traditional noble metal systems, this Ru/CeO_2 catalyst offers superior chemoselectivity and sustainability by eliminating the need for organic solvents.

This work not only demonstrates the efficacy of precisely engineered nanoclusters in aqueous biomass upgrading but also paves a sustainable path for transforming recalcitrant lignin intermediates into premium fine chemicals.

Electronic Supplementary Material: Supplementary material (experimental section, catalyst characterization images, and test results) is available in the online version of this article at https://doi.org/10.26599/NR.2026.94908659.

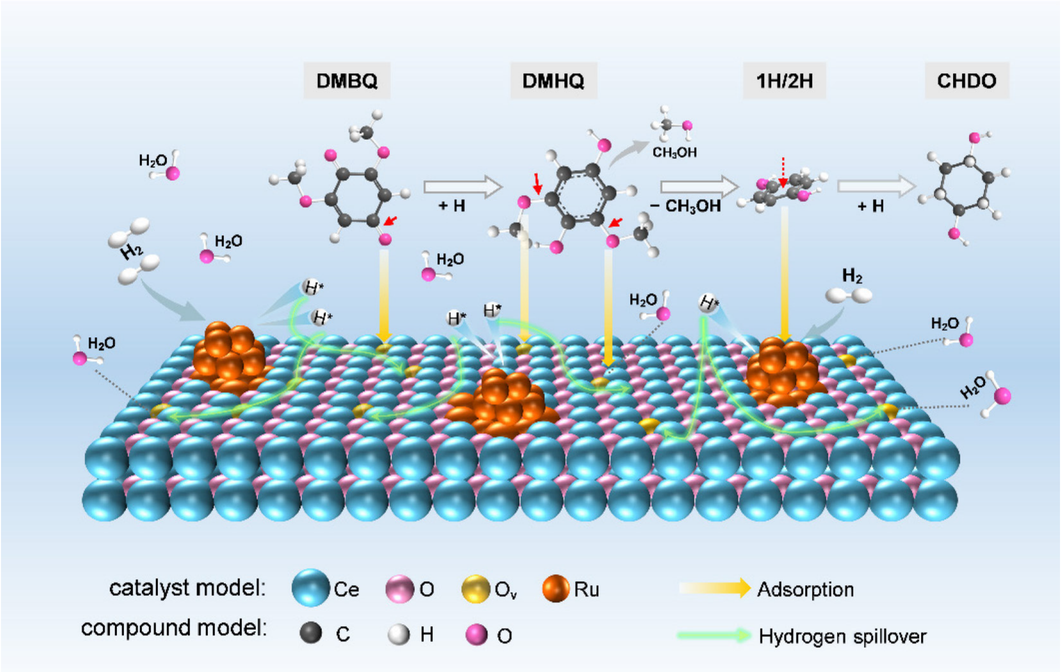

Figure 7 Proposed catalytic mechanism and energy profile for DMBQ HDO over Ru/CeO_2.

Data availability

All data needed to support the conclusions in the paper are presented in the manuscript and the Electronic Supplementary Material. Additional data related to this paper may be requested from the corresponding author upon request.

Acknowledgements

This work was support by the National Natural Science Foundation of China (Nos. 22378024 and 22101029), Beijing Municipal Natural Science Foundation (No. 2222006), Financial Program of BJAST (Nos. 25CA002 and 25CA011-02), and Scientific Research Program of BJAST (No. 25CB003-04).

Declaration of competing interest

All the contributing authors report no conflict of interests in this work.

Author contribution statement

Y. X. G. and J. L. C. conceived and designed the project. Y. X. G. performed the experiments and data analysis. X. Q. C., R. L., and Z. Z. S. carried out the NMR and GC measurements. Y. X. G., J. L. C, Z. H. S., and X. W. L. wrote and revised the manuscript. All the authors have approved the final manuscript.

Use of AI statement

None.

References

[1] Kobayashi, H.; Ohta, H.; Fukuoka, A. Conversion of lignocellulose into renewable chemicals by heterogeneous catalysis. *Catal. Sci. Technol.* **2012**, *2*, 869–883.

[2] Alonso, D. M.; Wettstein, S. G.; Dumesic, J. A. Bimetallic catalysts for upgrading of biomass to fuels and chemicals. *Chem. Soc. Rev.* **2012**, *41*, 8075–8098.

[3] Deng, W. P.; Feng, Y. C.; Fu, J.; Guo, H. W.; Guo, Y.; Han, B. X.; Jiang, Z. C.; Kong, L. Z.; Li, C. Z.; Liu, H. C. et al. Catalytic conversion of lignocellulosic biomass into chemicals and fuels. *Green Energy Environ.* **2023**, *8*, 10–114.

[4] Barker-Rothschild, D.; Chen, J. Q.; Wan, Z. M.; Renneckar, S.; Burgert, I.; Ding, Y.; Lu, Y.; Rojas, O. J. Lignin-based porous carbon adsorbents for CO_2 capture. *Chem. Soc. Rev.* **2025**, *54*, 623–652.

[5] Liu, W. J.; Yu, H. Q. Carbothermally synthesizing carbon nanostructures from biomass: A new paradigm for sustainable carbon materials production. *Environ. Sci. Technol.* **2025**, *59*, 24212–24232.

[6] Yan, L.; Huertas-Alonso, A. J.; Liu, H.; Dai, L.; Si, C. L.; Sipponen, M. H. Lignin polymerization: Towards high-performance materials. *Chem. Soc. Rev.* **2025**, *54*, 6634–6651.

[7] Zhang, B. W.; Qiang, G. R.; Barta, K.; Sun, Z. H. Bio-based polymers from lignin. *Innov. Mater.* **2024**, *2*, 100062.

[8] Li, W.; Sun, H.; Wang, G. H.; Sui, W. J.; Dai, L.; Si, C. L. Lignin as a green and multifunctional alternative to phenol for resin synthesis. *Green Chem.* **2023**, *25*, 2241–2261.

[9] Yuan, L. L.; Wang, H. M.; Wu, Y. C.; Hou, Q. X.; Sun, R. C. The booming lignin-derived functional composites/nanocomposites. *Compos. Part B: Eng.* **2024**, *287*, 111869.

[10] Liu, C.; Luan, P. C.; Li, Q.; Cheng, Z.; Xiang, P. Y.; Liu, D. T.; Hou, Y.; Yang, Y.; Zhu, H. L. Biopolymers derived from trees as sustainable multifunctional materials: A review. *Adv. Mater.* **2021**, *33*, 2001654.

[11] Zhang, C. F.; Shen, X. J.; Jin, Y. C.; Cheng, J. L.; Cai, C.; Wang, F. Catalytic strategies and mechanism analysis orbiting the center of critical intermediates in lignin depolymerization. *Chem. Rev.* **2023**, *123*, 4510–4601.

[12] Sun, Z. H.; Fridrich, B.; De Santi, A.; Elangovan, S.; Barta, K. Bright side of lignin depolymerization: Toward new platform chemicals. *Chem. Rev.* **2018**, *118*, 614–678.

[13] Schutyser, W.; Renders, T.; Van den Bosch, S.; Koelewijn, S. F.; Beckham, G. T.; Sels, B. F. Chemicals from lignin: An interplay of lignocellulose fractionation, depolymerisation, and upgrading. *Chem. Soc. Rev.* **2018**, *47*, 852–908.

[14] Wang, S. Z.; Li, X. C.; Ma, R. M.; Song, G. Y. Catalytic

hydrogenolysis of lignin into serviceable products. *Acc. Chem. Res.* **2025**, *58*, 529–542.

[15] Palumbo, C. T.; Ouellette, E. T.; Zhu, J.; Román-Leshkov, Y.; Stahl, S. S.; Beckham, G. T. Accessing monomers from lignin through carbon-carbon bond cleavage. *Nat. Rev. Chem.* **2024**, *8*, 799–816.

[16] Renders, T.; Van den Bosch, S.; Koelewijn, S. F.; Schutyser, W.; Sels, B. F. Lignin-first biomass fractionation: The advent of active stabilisation strategies. *Energy Environ. Sci.* **2017**, *10*, 1551–1557.

[17] Yu, X. N.; Wei, Z. Q.; Lu, Z. X.; Pei, H. S.; Wang, H. L. Activation of lignin by selective oxidation: An emerging strategy for boosting lignin depolymerization to aromatics. *Bioresour. Technol.* **2019**, *291*, 121885.

[18] Erickson, E.; Bleem, A.; Kuatsjah, E.; Werner, A. Z.; DuBois, J. L.; McGeehan, J. E.; Eltis, L. D.; Beckham, G. T. Critical enzyme reactions in aromatic catabolism for microbial lignin conversion. *Nat. Catal.* **2022**, *5*, 86–98.

[19] Huang, C. X.; Jiang, X.; Shen, X. J.; Hu, J. G.; Tang, W.; Wu, X. X.; Ragauskas, A.; Jameel, H.; Meng, X. Z.; Yong, Q. Lignin-enzyme interaction: A roadblock for efficient enzymatic hydrolysis of lignocellulosics. *Renew. Sustain. Energy Rev.* **2022**, *154*, 111822.

[20] Gao, D. H.; Ouyang, D. H.; Zhao, X. B. Electro-oxidative depolymerization of lignin for production of value-added chemicals. *Green Chem.* **2022**, *24*, 8585–8605.

[21] Gao, Z. Y.; Ren, P. N.; Sun, L. L.; Luo, N. C.; Wang, F. Photocatalysts for steering charge transfer and radical reactions in biorefineries. *Nat. Synth.* **2024**, *3*, 438–451.

[22] Nguyen, T. V. T.; Kim, S.; Yoo, C. G.; Choi, J. W.; Leem, G.; Kim, Y. H. Lignin peroxidase-catalyzed selective cleavage of C–C bonds in lignin at room temperature. *ACS Catal.* **2024**, *14*, 11733–11740.

[23] Subbotina, E.; Rukkijakan, T.; Marquez-Medina, M. D.; Yu, X. W.; Johnsson, M.; Samec, J. S. M. Oxidative cleavage of C–C bonds in lignin. *Nat. Chem.* **2021**, *13*, 1118–1125.

[24] Stärk, K.; Taccardi, N.; Bösmann, A.; Wasserscheid, P. Oxidative depolymerization of lignin in ionic liquids. *ChemSusChem* **2010**, *3*, 719–723.

[25] Wu, X. Y.; De Bruyn, M.; Hulan, J. M.; Brasil, H.; Sun, Z. H.; Barta, K. High yield production of 1,4-cyclohexanediol and 1,4-cyclohexanediamine from high molecular-weight lignin oil. *Green Chem.* **2023**, *25*, 211–220.

[26] Zhang, Z. H.; Wu, X. Y.; Ren, X. H.; Rong, Z. M.; Sun, Z. H.; Barta, K.; Yuan, T. Q. High yield production of 1,4-cyclohexanediol from lignin derived 2,6-dimethoxybenzoquinone via Raney NiMn catalyst in hydrogen free conditions. *J. Energy Chem.* **2023**, *83*, 275–286.

[27] Bian, S.; Pagan, C.; Andrianova "Artemyeva", A. A.; Du, G. D. Synthesis of polycarbonates and poly(ether carbonate)s directly from carbon dioxide and diols promoted by a Cs_2CO_3/CH_2Cl_2 system. *ACS Omega* **2016**, *1*, 1049–1057.

[28] Asaad, J. N.; Abd-El-Messieh, S. L. Effect of glycol and filler types on some polymeric composite properties. *J. Appl. Polymer Sci.* **2008**, *109*, 1916–1924.

[29] Moon, J. I.; Lee, Y. H.; Kim, H. J. Synthesis and characterization of elastomeric polyester coatings for automotive pre-coated metal. *Prog. Org. Coat.* **2012**, *74*, 125–133.

[30] Rosado, M. T. S.; Maria, T. M. R.; Castro, R. A. E.; Canotilho, J.; Silva, M. R.; Eusébio, M. E. S. Molecular structure and polymorphism of a cyclohexanediol: *Trans*-1,4-cyclohexanedimethanol. *CrystEngComm* **2014**, *16*, 10977–10986.

[31] He, Q.; Zhou, Y. Z.; Shou, H. W.; Wang, X. Y.; Zhang, P. J.; Xu, W. J.; Qiao, S. C.; Wu, C. Q.; Liu, H. J.; Liu, D. B. et al. Synergic reaction kinetics over adjacent ruthenium sites for superb hydrogen generation in alkaline media. *Adv. Mater.* **2022**, *34*, 2110604.

[32] Liu, Y.; Liu, S. L.; Wang, Y.; Zhang, Q. H.; Gu, L.; Zhao, S. C.; Xu, D. D.; Li, Y. F.; Bao, J. C.; Dai, Z. H. Ru modulation effects in the synthesis of unique rod-like $Ni@Ni_2P$–Ru heterostructures and their remarkable electrocatalytic hydrogen evolution performance. *J. Am. Chem. Soc.* **2018**, *140*, 2731–2734.

[33] Qin, Q.; Jang, H.; Chen, L. L.; Nam, G.; Liu, X. E.; Cho, J. Low loading of Rh_xP and RuP on N, P codoped carbon as two trifunctional electrocatalysts for the oxygen and hydrogen electrode reactions. *Adv. Energy Mater.* **2018**, *8*, 1801478.

[34] An, Z. Y.; Xue, H.; Sun, J.; Guo, N. K.; Song, T. S.; Sun, J. W.; Hao, Y. R.; Wang, Q. Co-construction of sulfur vacancies and heterogeneous interface into Ni_3S_2/MoS_2 catalysts to achieve highly efficient overall water splitting. *Chin. J. Struct. Chem.* **2022**, *41*, 2208037–2208043.

[35] Guan, S. Y.; Liu, Y. Y.; Liu, S. L.; Zhuang, Z. C.; Shen, R. F.; Zhang, H. H.; Liang, E. J.; Fan, Y. P.; Jiang, J. C.; Liu, B. Z. et al. MXene-supported Ru-Ni: A common active site for hydrolysis, hydrogen oxidation, and hydrogenation. *Angew. Chem., Int. Ed.* **2025**, *64*, e202506869.

[36] Gan, Q.; Zhou, W. H.; Zhang, X. P.; Lin, Y. M.; Huang, S. L.; Lu, G. P. Selective hydrodeoxygenation of lignin-derived phenolic monomers to cyclohexanol over tungstated zirconia supported ruthenium catalysts. *ChemSusChem* **2024**, *17*, e202400644.

[37] Luo, Q. S.; Wang, H.; Lv, Y. T.; Fan, J. H.; Wu, H. X.; Fang, W.; Liu, L. J.; Liu, P.; Wang, L.; Xiao, F. S. Hydrophobic poly(divinylbenzene) polymer-supported ruthenium catalysts for efficient hydrogenation of pyridines in water. *Angew. Chem., Int. Ed.* **2025**, *64*, e202510284.

[38] Zhao, Y. Y.; Zhan, J. H.; Hu, R.; Luo, G.; Fan, J. J.; Clark, J. H.; Zhang, S. C. Water-assisted catalytic transfer hydrogenation of guaiacol to cyclohexanol over $Ru/NiAl_2O_4$. *Chem. Eng. J.* **2024**, *485*, 149934.

[39] Chen, X.; Zheng, Y. N.; Zhang, Q.; Qiu, S. B.; Meng, Q. W.; Wu, X. P.; Wang, T. J. Controlling transformation of sorbitol into 1-hexanol over $Ru-MoO_x/Mo_2C$ catalyst via aqueous-phase hydrodeoxygenation. *ACS Sustainable Chem. Eng.* **2021**, *9*, 9033–9044.

[40] Han, Z. K.; Liu, W.; Gao, Y. Advancing the understanding of oxygen vacancies in ceria: Insights into their formation, behavior, and catalytic roles. *JACS Au* **2025**, *5*, 1549–1569.

[41] Liu, L. C.; Corma, A. Metal catalysts for heterogeneous catalysis: From single atoms to nanoclusters and nanoparticles. *Chem. Rev.* **2018**, *118*, 4981–5079.

[42] Xu, M.; Peng, M.; Tang, H. L.; Zhou, W.; Qiao, B. T.; Ma, D. Renaissance of strong metal–support interactions. *J. Am. Chem. Soc.* **2024**, *146*, 2290–2307.

[43] Zhao, S. Z.; Kang, D. J.; Liu, Y. P.; Wen, Y. F.; Xie, X. Z.; Yi, H. H.; Tang, X. L. Spontaneous formation of asymmetric oxygen vacancies in transition-metal-doped CeO_2 nanorods with improved activity for carbonyl sulfide hydrolysis. *ACS Catal.* **2020**, *10*, 11739–11750.

[44] Shang, Y. X.; Yue, W. H.; Liu, Z. H.; Zhang, R. Y.; Ge, Q. F.; Zhu, X. L. Facet-dependent metal–support interactions of Ru/CeO_2 dictate the activity for direct deoxygenation of m-cresol. *Fuel* **2026**, *410*, 137966.

[45] Tang, B.; Ji, Q. Q.; Zhang, X. L.; Shi, R. C.; Ma, J.; Zhuang, Z. C.; Sun, M.; Wang, H. J.; Liu, R. Q.; Liu, H. J. et al. Symmetry breaking of FeN_4 moiety via edge defects for acidic oxygen reduction reaction. *Angew. Chem.* **2025**, *137*, e202424135.

[46] Dai, Q. G.; Huang, H.; Zhu, Y.; Deng, W.; Bai, S. X.; Wang, X. Y.; Lu, G. Z. Catalysis oxidation of 1,2-dichloroethane and ethyl acetate over ceria nanocrystals with well-defined crystal planes. *Appl. Catal. B: Environ.* **2012**, *117–118*, 360–368.

[47] Sivan, S. E.; Kang, K. H.; Han, S. J.; Okello, O. F. N.; Choi, S. Y.; Sudheeshkumar, V.; Scott, R. W. J.; Chae, H. J.; Park, S.; Lee, U. H. Facile MOF-derived one-pot synthetic approach toward Ru single atoms, nanoclusters, and nanoparticles dispersed on CeO_2 supports for enhanced ammonia synthesis. *J. Catal.* **2022**, *408*, 316–328.

[48] Liu, L. J.; Yao, Z. J.; Deng, Y.; Gao, F.; Liu, B.; Dong, L. Morphology and crystal-plane effects of nanoscale ceria on the activity of CuO/CeO_2 for NO reduction by CO. *ChemCatChem* **2011**, *3*, 978–989.

[49] Xiao, C. X.; Goh, T. W.; Qi, Z. Y.; Goes, S.; Brashler, K.; Perez, C.; Huang, W. Y. Conversion of levulinic acid to γ-valerolactone over few-layer graphene-supported ruthenium catalysts. *ACS Catal.* **2016**, *6*, 593–599.

[50] Gao, Y.; Yang, C. D.; Sun, F. L.; He, D. P.; Wang, X. Q.; Chen, J.; Zheng, X. B.; Liu, R. C.; Pan, H. G.; Wang, D. S. Ligand-tuning metallic sites in molecular complexes for efficient water oxidation. *Angew. Chem., Int. Ed.* **2025**, *64*, e202415755.

[51] Wang, Z.; Huang, Z. P.; Brosnahan, J. T.; Zhang, S.; Guo, Y. L.; Guo, Y.; Wang, L.; Wang, Y. S.; Zhan, W. C. Ru/CeO_2 catalyst with optimized CeO_2 support morphology and surface facets for propane combustion. *Environ. Sci. Technol.* **2019**, *53*, 5349–5358.

[52] Huang, H.; Dai, Q. G.; Wang, X. Y. Morphology effect of Ru/CeO_2 catalysts for the catalytic combustion of chlorobenzene. *Appl. Catal. B: Environ.* **2014**, *158–159*, 96–105.

[53] Zhao, J.; Gao, G.; Li, T.; Deng, Y. T.; Wang, B.; Dai, P. H.; Li, H. S.; Zhuang, Z. C.; Yang, J. R.; Wang, J. Z. et al. Single atom-substituted chalcogenides with anion vacancy bonded on graphene nanotubes for achieving “1 + 1 + 1 > 3” synergistic enhanced sodium storage. *Angew. Chem.* **2025**, *137*, e202512028.

[54] Tang, Y. X.; Wang, H.; Guo, C.; Wang, L. G.; Zhao, T. T.; Xiao, S. K.; Liu, J. R.; Jiang, Y. Y.; Zhao, Y. F.; Wen, X. D. et al. Synergies between atomically dispersed ru single atoms and nanoparticles on $CeAlO_x$ for enhanced photo-thermal catalytic CO_2 hydrogenation. *Adv. Mater.* **2026**, *38*, e12793.

[55] Zhang, X. Q.; Qi, Y. Q.; Liu, H.; Wang, J. Y.; Xie, L. Y.; Shi, J. L.; Wang, F.; Liu, Y. L.; Wang, Z. X.; Guo, A. J. Anchored Ru nanoclusters strategy enhances hydrogen spillover effect for high-efficiency hydrogen storage. *Chem. Eng. J.* **2024**, *498*, 155203.

[56] Yang, H. C.; Duan, P. F.; Zhuang, Z. C.; Luo, Y. W.; Shen, J.; Xiong, Y. L.; Liu, X. W.; Wang, D. S. Understanding the dynamic evolution of active sites among single atoms, clusters, and nanoparticles. *Adv. Mater.* **2025**, *37*, 2415265.

[57] Zhu, S. H.; Wu, R. Q.; Li, X. M.; Dong, M.; Fan, W. B. Reactive interfacial oxygen vacancies in Ru/TiO_2 for efficient reductive amination of bio-based carbonyl compounds. *Chem. Eng. J.* **2026**, *527*, 171752.

[58] Ding, K.; Zhang, J. H.; Xu, D. L.; Hang, J. F.; Kontchouo, F. M. B.; Thanachayanont, C.; Lampang, T. N.; Xu, Z. Y.; Zhang, S.; Ruan, R. Unraveling role of oxygen vacancies in catalytic deoxygenation of biomass-derived carboxylic acids over ceria. *Bioresour. Technol.* **2026**, *439*, 133349.

[59] Wang, Y.; Yu, H. C.; He, Y. R.; Xiang, S. L.; Qin, X. T.; Yang, L. N.; Chen, J. W.; Si, Y.; Zhang, J. W.; Diao, J. Y. et al. Fully exposed Ru clusters for the efficient multi-step toluene hydrogenation reaction. *Angew. Chem., Int. Ed.* **2025**, *64*, e202415542.